

Camera Splatting for Continuous View Optimization

Gahye Lee Hyomin Kim Gwangjin Ju Joeeun Son Hyejeong Yoon Seungyong Lee

POSTECH

{gahye0509, min00001, gwangjin, jeson, hgyoon02, leesy}@postech.ac.kr

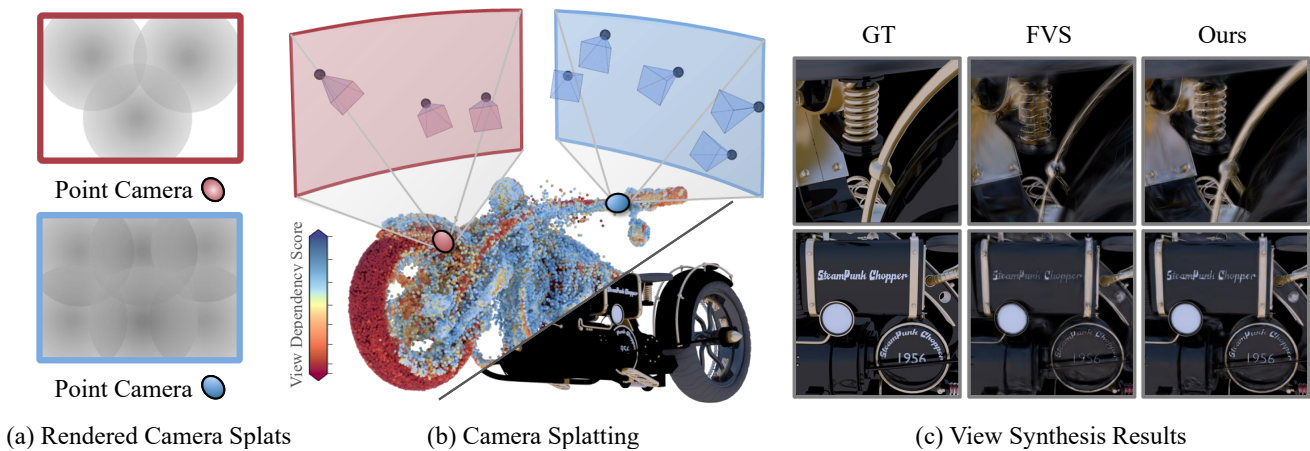


Figure 1. We propose *Camera Splatting*, a novel view optimization framework for novel view synthesis. Each camera is modeled as a 3D Gaussian, referred to as a *camera splat*, and virtual cameras, termed *point cameras*, are placed at 3D points sampled near the surface to observe the distribution of camera splats. View optimization is achieved by *continuously and differentiably* refining the camera splats so that desirable target distributions are observed from the point cameras, in a manner similar to the original 3D Gaussian splatting. Compared to the Farthest View Sampling (FVS) approach, our optimized views demonstrate superior performance in capturing complex view-dependent phenomena, including intense metallic reflections and intricate textures such as text.

Abstract

Given limited camera budgets, identifying informative views is essential for effectively reconstructing a radiance field to achieve high-quality novel view synthesis. These views should adaptively sample the radiance field based on the geometry and view-dependent appearance of the scene. Existing methods typically optimize views by selecting from a predefined camera set or adopting a greedy next-best-view strategy, limiting the flexibility and accuracy of the optimization. In this paper, we propose a novel continuous view optimization framework, called *Camera Splatting*, which enables joint optimization of multiple views. Our key idea is to represent each camera as a specialized 3D Gaussian (*camera splat*), allowing for gradient-based optimization within a continuous camera parameter space. To evaluate view optimality, we introduce virtual cameras (*point*

cameras) placed at sampled points in the scene, which render camera splats and provide feedback on their spatial positions and orientations. The resulting optimized views effectively capture the view-dependent appearance of the scene at the sampled points. Integrated into a Gaussian splatting pipeline, our approach can efficiently and simultaneously optimize a large number of views. Quantitative and qualitative evaluations demonstrate the effectiveness of the views optimized by *Camera Splatting* for novel view synthesis under a limited camera budget.

1. Introduction

Novel view synthesis aims to generate unseen views of a 3D scene from a limited set of captured images. Central to this task is the radiance field, a continuous representation

encoding both scene geometry and view-dependent appearance [1, 8, 13, 21]. Formally, a radiance field is defined as a continuous mapping from a 5D input space, consisting of 3D spatial coordinates x and 2D directions ω , to color c and density σ .

Reconstructing a radiance field requires sampling across both x and ω . In practice, this sampling is achieved by capturing images from various camera views. A dense and uniform capture would yield the ideal and best reconstruction. However, constraints such as a limited camera budget and computational resource make this approach impractical. Selecting the most informative views is essential for efficiently capturing the radiance field, enabling high-quality novel view synthesis under a limited camera budget [9, 14, 17, 19, 23].

Early researches on view optimization focused on geometry reconstruction with constraints from multi-view geometry [28, 33]. With recent advancements in novel view synthesis, view optimization methods prioritize improving the quality of novel view synthesis. They measure the quality of the reconstructed radiance field to identify regions that require additional sampling [9, 23]. However, the optimization strategies of previous methods often yield suboptimal results. Some methods use discrete optimization that selects views from a predefined set of candidate camera positions [9, 14, 23, 30], which limits flexibility in the solution space. Others employ a greedy next-best-view optimization strategy [5, 16, 19, 32], iteratively selecting views one by one. It improves the efficiency of view selection but could result in local optima.

Ideally, a view optimization strategy should provide adaptive and balanced sampling of the radiance field for the target scene. The strategy should also support continuous and flexible exploration of the camera parameter space, eliminating the need for a predefined set of cameras. In addition, all camera views should be optimized simultaneously, avoiding local minima that may arise from a greedy next-best-view approach. Computational efficiency and scalability are also essential to handle a large number of optimized views.

In this paper, we present *Camera Splatting*, a novel view optimization framework inspired by 3D Gaussian Splatting (3DGS) [13], which supports continuous and joint optimization of multiple cameras. Our core innovation is to represent each camera as a specialized 3D Gaussian, called a *camera splat*, that encodes optimizable camera parameters for adaptively sampling the radiance field. We also introduce virtual cameras, termed *point cameras*, which are strategically placed at sampled points in the scene to evaluate the current radiance field sampling achieved by the camera splats. Leveraging the efficient and fully differentiable 3DGS optimization pipeline, our framework directly optimizes camera parameters by rendering camera splats from

point cameras, enabling continuous, efficient, and scalable optimization that can handle a large number of cameras simultaneously.

We validate our Camera Splatting framework by employing it to select optimal views for 3D Gaussian Splatting of both object and scene scales. We demonstrate the effectiveness of our framework through quantitative and qualitative evaluations on various camera configurations. We also show that view-dependent effects, even in a scene with complex materials and detailed textures, can be accurately captured by our optimized views.

In summary, our main contribution is proposing a novel continuous view optimization framework, *Camera Splatting*, designed for a high-quality novel view synthesis, which consists of:

- A novel view representation using a 3D Gaussian, *camera splat*, that allows for continuous and differential optimization of camera parameters.
- A novel virtual camera model, *point camera*, that enables the evaluation of the radiance field sampling achieved by camera splats
- A continuous, efficient, and scalable optimization process, capable of simultaneously handling a large number of cameras, inspired by 3DGS.

2. Related Work

View optimization methods have been extensively studied. Early methods focused on geometry reconstruction, guided by techniques such as multi-view geometry or stereo matching. With advances in novel view synthesis, recent methods focus on optimizing view selection for high-quality radiance field reconstruction.

View optimization for geometry reconstruction The main goal of view optimization methods for geometry reconstruction is to maximize coverage, ensuring sufficient geometric constraints between views [7, 15, 20, 27, 33]. For example, Aerial Path Planning (APP) [28] introduces reconstructability heuristics for stereo matching by leveraging pairwise relationships among views. While APP leverages the downhill simplex method to optimize the view set, Offsite Aerial Path Planning (OAPP) [33] employs bundle adjustment for the optimization. Submodular [25] proposes local surface coverage through angular diversity and selects the best trajectories to maximize global scene coverage. Although these geometry-driven approaches effectively capture the complete surface, they do not consider view-dependent appearances needed for novel view synthesis.

View optimization for novel view synthesis To identify optimal views for novel view synthesis, several studies have

proposed uncertainty metrics on radiance fields [10, 12, 16, 24, 26, 29]. FisherRF [9] leverages Fisher Information derived from the Hessian matrix of the loss function to select views that maximize information gain. ActiveNeRF [23] defines uncertainty as color variance estimated from each spatial position and trains the variance using NeRF [21] framework. Manifold sampling [19] models the radiance field using stochastic variables, considering the sampling variance as an uncertainty measure to optimize the view. Recently, Kopanas and Drettakas [14] proposed an alternative by explicitly considering observation frequency and angular uniformity to achieve balanced view frequency and directional diversity.

These approaches address view-dependent appearance implicitly through radiance field uncertainty measures. In contrast, our framework explicitly considers view dependency in the optimization process, directly improving sampling of viewing directions. This ensures high-quality radiance field reconstructions with accurate view-dependent details.

Optimization strategies Different strategies have been adopted to identify optimal views based on various definitions of view optimality. For computational efficiency and straightforward implementation, most existing methods rely on discrete optimization such as view selection from candidate views [2, 6, 9, 14, 23, 31, 33]. This approach can restrict solution optimality due to the fixed candidate camera set. Furthermore, the combinatorial complexity of this optimization grows exponentially with the number of views being optimized. To manage the complexity, Roberts et al. [25] separately optimized rotation and translation parameters, which increases the risk of suboptimal solutions.

Alternatively, continuous optimization has also been adopted for flexible exploration of the solution space. APP [28] incrementally optimizes the camera configuration by randomly selecting and optimizing one view at a time in the continuous parameter space. Manifold Sampling [19] proposes a differentiable uncertainty metric for radiance fields, enabling gradient-based optimization of individual views. However, these approaches optimize views with a greedy strategy that can fall into local optima.

Our framework addresses these limitations by simultaneously optimizing multiple camera views within a continuous parameter space. Leveraging 3DGS-inspired optimization, our framework achieves efficient and scalable joint optimization, effectively avoiding locally optimal solutions.

3. Radiance Field Sampling

3.1. Radiance Field

A *Radiance Field* is a core concept for representing the appearance of a 3D scene in a volumetric manner, which can

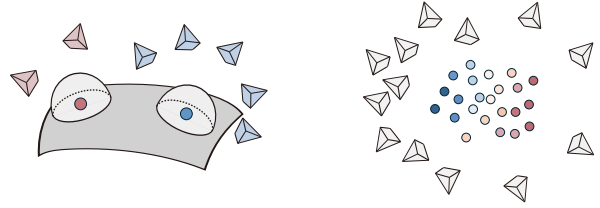


Figure 2. Illustration of sampling density and view optimality. In both images, red circles indicate regions with weak view dependency, while blue circles represent regions with strong view dependency. As shown in the left image, sampling should concentrate near surfaces, with density adapting to local view dependency. The right image visualizes an ideal view configuration, where the view distribution effectively captures the target surface with adaptive sampling density based on view-dependency.

be defined by:

$$F_\theta : (\mathbf{x}, \omega) \mapsto (\sigma, \mathbf{c}), \quad (1)$$

where $\mathbf{x} \in \mathbb{R}^3$ is a position vector, $\omega \in \mathbb{S}^2$ is a viewing direction vector, and the output consists of a volumetric density $\sigma \in \mathbb{R}$ and a view-dependent color $\mathbf{c} \in \mathbb{R}^3$.

Recently, 3D Gaussian Splatting (3DGS) [13] is proposed to represent the radiance field effectively. In 3DGS, each 3D Gaussian is characterized by parameters such as a position μ_i , a covariance matrix Σ_i , opacity α_i , and color \mathbf{c}_i represented with spherical harmonics. For rendering, these primitives are projected onto the 2D image plane, and their colors are combined using alpha blending. They approximate the volume rendering equation [11], reducing to a simpler expression:

$$L_o(r) = \sum_{i=1}^N T_i \alpha_i \mathbf{c}_i, \quad T_i = \prod_{j=1}^{i-1} (1 - \alpha_j), \quad (2)$$

where the $L_o(r)$ represents the rendered radiance along ray r , and T_i denotes the accumulated transmittance. This approach enables fully differentiable rendering for efficient parameter update.

3.2. View Optimality for Radiance Field Sampling

Accurate radiance field reconstruction requires appropriate sampling in both the spatial domain x and the viewing directional domain ω . However, dense sampling in both domains is often impractical due to limited resources. View selection needs to focus on important position and direction with an effective sampling strategy.

In the spatial domain x , sampling should focus on regions of interest in the scene, which would primarily be the scene surfaces. The sampling in the directional domain ω for a given position x should cover all viewing directions,

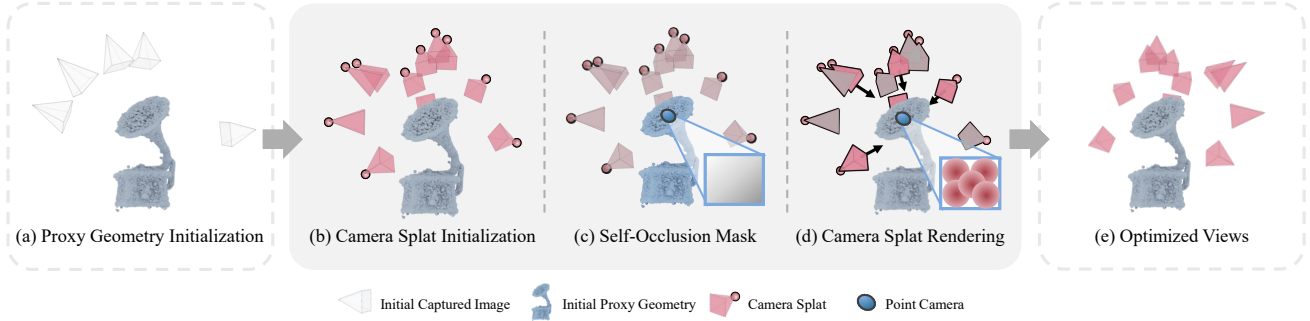


Figure 3. Overall process of view optimization using our Camera Splatting framework, highlighting the initialization, core components of the framework, and the resulting optimized view configuration.

and the sampling density should adapt to the local view-dependent appearance. For example, reflective surfaces demand denser directional sampling compared to matte surfaces. As illustrated in Fig. 2, optimal sampling positions are placed near scene surfaces, with varying sampling densities depending on the view dependency.

With these desired sampling properties, we define optimal views as cameras whose emitted view rays best approximate the target sampling of both positions and viewing directions in the radiance field. Optimal views should cover all viewing directions at surface points, while the sampling density in viewing directions should increase with the view-dependency of surface points.

4. Camera Splatting

We introduce *Camera Splatting*, a novel continuous and efficient view optimization framework inspired by 3DGS. Given a proxy geometry and view dependency information on the geometry, our framework simultaneously optimizes all camera views to adaptively sample the radiance field.

4.1. Camera Splat

In Camera Splatting, we model the physical cameras as specialized 3D Gaussians called *camera splats* C . Each camera splat encodes both extrinsic and intrinsic properties of a camera. These include its center position μ , rotation vector r , uniform scale s , field-of-view (FoV) θ , and opacity α :

$$C_i = \{\mathbf{u}_i, \mathbf{r}_i, s, \theta, \alpha\}. \quad (3)$$

Here, FoV θ and opacity α are fixed constants, and the scale parameter s is a shared scalar across all camera splats. These shared parameters help identify overly clustered views and maintain directional uniformity during optimization. The detailed rationale on this design choice is discussed in Section 5.

4.2. Point Camera

We evaluate the camera splats by rendering them from virtual cameras called *point cameras* P . Each point camera is omnidirectional, allowing it to measure the directional sampling density from all visible views at its position.

Point cameras are positioned on the proxy geometry to represent regions of interest that likely contain scene surfaces. They also utilize the local view dependency information of the proxy geometry. Details on the initialization of point cameras are provided in the supplementary material.

4.3. Camera Splat Rendering at Point Camera

We render the opacity values of camera splats from point cameras, based on the 3DGS rendering pipeline. During the rendering process, we apply a binary visibility mask based on FoV θ and orientation r of each camera splat. A camera splat is considered visible from a point camera if the angle between the camera splat’s orientation vector r_i and the vector v_i pointing from the camera splat to the point camera is within $\frac{\theta}{2}$. Based on Eq. (2), our modified rendering equation for a ray \hat{r} from a point camera P_i is defined as:

$$I_{render}(\hat{r}) = \sum_{i=1}^N T_i \alpha_i m_i \quad T_i = \prod_{j=1}^{i-1} (1 - \alpha_j m_j) \quad (4)$$

$$\text{where } m_i(P_i) = \begin{cases} 1 & \text{if } \angle(v_i, r_i) \leq \frac{\theta}{2} \\ 0 & \text{otherwise} \end{cases}.$$

Since camera splats share a fixed opacity value, the rendered image reflects both the coverage and density of the directional sampling. Higher image intensities indicate more overlapping camera splats, implying dense sampling of view directions, while zero intensity implies no sampling around that viewing direction.

Rendering camera splats from a point camera P_i may mistakenly include those occluded by the proxy scene geometry. To address this, we introduce a self-occlusion mask $I_{occ}(P_i)$, computed by rendering the proxy geometry from each point camera P_i (Fig. 4). This mask is applied to the



Figure 4. Visualization of the self-occlusion mask (Section 4.3) and the estimated View-Dependency Score (VDS) (Section 5.2). (left) For a given point camera, the self-occlusion mask captures visibility considering proxy geometry occlusions. (right) The VDS is computed for each point camera to determine the optimal viewing direction sampling density.

rendered camera splats during optimization, effectively reducing the influence of self-occluded camera splats.

5. Continuous View Optimization

Our optimization goal is to identify camera views that effectively sample the radiance field with adaptive density of view directions using the proxy geometry and its view-dependency information. To achieve this, we ensure that each point on the proxy geometry is observed uniformly from all viewing directions, with the sampling density adapted to its local view-dependency characteristics.

5.1. Ground Truth Image

For each point camera, we define the ideal camera splat configuration as being distributed uniformly over all viewing directions emitting from the point camera. As noted in Section 4.3, the pixel intensity rendered at a point camera reflects the density of camera splats in each viewing direction. Consequently, a rendered image with uniform pixel intensity suggests that the camera splats are evenly distributed across viewing directions. Based on this observation, we define a base ground truth image I_{base} to be a monochromatic image with constant intensity equal to the fixed opacity of camera splats.

5.2. View Dependency Score

Different materials exhibit unique reflectance properties, requiring varying sampling densities across viewing directions. To achieve this, we introduce a *View-Dependency Score Function (VDSF)*, a predefined function that estimates the view dependency of each point on the proxy geometry (Fig. 4). The function indicates the relative directional sampling density needed at each point, enabling adaptive allocation of views within a fixed camera budget.

We control the desired sampling density at each point camera P_i by scaling the base ground truth image I_{base} with the estimated view-dependency score:

$$I_{gt}(P_i) = \text{VDSF}(P_i) \times I_{base}. \quad (5)$$

This VDSF-based scaling strategy directly controls the angular spacing between camera splats at each point camera P_i . Higher I_{gt} values lead to increased overlaps among projected camera splats, resulting in higher sampling density of viewing directions for P_i .

In this paper, we define the VDSF as a data-driven cubic polynomial function. Details of the VDSF are provided in the supplementary material.

5.3. Gradient-based View Optimization

Image loss Given N point cameras and camera splats C , we define the image loss $\mathcal{L}_{\text{image}}$ as the Mean Squared Error (MSE) between the rendered camera splat images I_{render} and the ground truth images I_{gt} . To account for self-occlusions, we multiply the pixel-wise difference by the occlusion mask I_{occ} :

$$\mathcal{L}_{\text{image}} = \frac{1}{N} \sum_{i=1}^N \|(I_{\text{render}}(P_i) - I_{\text{gt}}(P_i)) \odot I_{\text{occ}}(P_i)\|_2^2. \quad (6)$$

However, directly optimizing with this image loss raises two issues: (1) If the scale of each camera splat is not globally coherent, the optimization can trivially adjust individual scales to match intensity targets (e.g., one big camera splat and others with zero scale) without achieving directional uniformity. (2) The projected image-space scales of camera splats can be manipulated with perspective foreshortening by adjusting the depths from the point camera. Then, optimization can meet intensity requirements through adjusting individual scales or depths, rather than improving angular uniformity.

To prevent these undesirable solutions, we set the global scale parameter to be shared among all camera splats, ensuring each camera splat to have a similar projected area. Additionally, we normalize the scale of each camera splat based on its depth from the point camera P_i . This normalization mitigates perspective foreshortening, encouraging that all camera splats have identical scales in image space. As a result, optimization genuinely targets directional uniformity.

Directional regularizer To ensure that camera splats orient toward scene surfaces without causing under-covered regions, we introduce a regularization term that encourages orientations of the camera splats to align with the surface parts they observe.

For the i -th point camera P_i and the j -th camera splat C_j , we calculate the cosine similarity between the vector v_i which directs from P_i to C_j , and the camera splat's rotation vector r_j . The directional regularizer is defined as:

$$\mathcal{L}_{\text{reg}} = \sum_{i=1}^N \sum_{j=1}^M m_{\text{occ}}^{(i)} w(i) \cos\text{Sim}(\mathbf{r}_j, \mathbf{v}_i), \quad (7)$$

where $m_{occ}^{(i)}$ is a weight derived from the self-occlusion mask I_{occ} of the i -th point camera for the ray v_i , and $w(i)$ is a coverage weight for P_i . We assign a high value to the weight w for a point camera with lower coverage, encouraging camera splats to orient towards the point cameras with low sampling density. Detailed formulation of the coverage weight is provided in the supplementary material.

Boundary regularizer We apply a boundary regularizer \mathcal{L}_{bound} that penalizes camera splats deviating from a pre-defined boundary range. This regularization helps prevent camera splats from drifting into invalid regions where they are not visible to any point cameras and become unused during optimization. See the supplementary for detailed formulation.

Final loss We define the final loss function as the sum of the image loss and the regularizers:

$$\mathcal{L}_{total} = \mathcal{L}_{image} + \mathcal{L}_{reg} + \mathcal{L}_{bound}. \quad (8)$$

Since our framework is fully differentiable, camera splats C are optimized by directly minimizing L_{total} .

6. View Optimization Using 3DGS

Our framework can optimize views for high-quality radiance field reconstruction, given proxy geometry and view dependency information defined over the proxy geometry. The proxy geometry can be obtained through various methods, including NeRF [21], 3D Gaussian Splatting (3DGS) [13], and 3D reconstruction methods (e.g., Kinect-Fusion [22]). Once optimized, the selected views can be used for a range of radiance field reconstruction frameworks, including NeRF and 3DGS.

In this paper, for our experiments, we adopt 3DGS to reconstruct high-quality radiance fields, due to its recent widespread adoption. We also use 3DGS to build the proxy geometry for view optimization.

We reconstruct a proxy geometry by optimizing a 3DGS scene using sparse input images and their associated camera poses. Point cameras are then placed on the Gaussian primitives of the optimized 3DGS, and the view dependency information is obtained for each point camera by computing VDSF using the sparse input images. Camera splats are randomly initialized around the proxy geometry obtained by 3DGS.

During each optimization iteration, a subset of point cameras is sampled, and camera splats are rendered from the sampled point cameras to evaluate the directional sampling densities. Before optimization, camera splats are created from the views used for capturing the sparse input images, and they remain fixed during the optimization process

	50 cameras			150 cameras		
	PSNR \uparrow	SSIM \uparrow	LPIPS \downarrow	PSNR \uparrow	SSIM \uparrow	LPIPS \downarrow
Manifold	25.99	0.850	0.146	26.47	0.866	0.136
FVS	26.20	0.866	0.140	26.72	0.880	0.130
Ours (w/o VDS)	26.50	0.874	0.227	27.26	0.891	0.120
Ours	27.05	0.883	0.126	28.46	0.910	0.106

Table 1. Quantitative comparison on close-view renderings for the test set of the NSVF dataset.

	50 cameras			150 cameras		
	PSNR \uparrow	SSIM \uparrow	LPIPS \downarrow	PSNR \uparrow	SSIM \uparrow	LPIPS \downarrow
Manifold	32.82	0.967	0.031	33.23	0.970	0.030
FVS	33.10	0.972	0.027	33.77	0.976	0.026
Ours (w/o VDS)	32.99	0.972	0.027	33.67	0.975	0.026
Ours	32.74	0.970	0.028	33.19	0.973	0.025

Table 2. Quantitative comparison on far-view renderings for the test set of the NSVF dataset.

	Indoor Christmas scene			Minimal room scene		
	PSNR \uparrow	SSIM \uparrow	LPIPS \downarrow	PSNR \uparrow	SSIM \uparrow	LPIPS \downarrow
Random	32.00	0.896	0.152	34.29	0.942	0.288
Ours (w/o VDS)	32.43	0.899	0.146	34.33	0.950	0.274
Ours	33.92	0.918	0.123	34.06	0.948	0.274

Table 3. Quantitative comparison on the test set of the BlenderKit dataset.

to prevent the optimized views from overlapping with the initial views.

Once the optimized camera splats are obtained, the scene is re-scanned for a high-quality 3DGS reconstruction. Detailed pseudocode and additional training strategies are provided in the supplementary material.

This view optimization scenario can be applied to diverse radiance field reconstruction tasks. For example, in large-scale environments where manual assessment is challenging, an autonomous system can first capture a small set of rough images. Our algorithm then suggests additional optimal camera placements to the robot. This approach enables an efficient, scalable, and fully automated scene acquisition workflow.

7. Experiments

7.1. Experimental Setting

We evaluate our method against two recent view optimization methods: Farthest View Sampling (FVS) and Manifold Sampling [19]. FVS demonstrated the state-of-the-art performance in NeRF Director [30], while Manifold Sampling represents the state-of-the-art in continuous view optimization. Additionally, we compare our method with and without VDSF to demonstrate its effectiveness.

We conduct comparisons using the Synthetic-NSVF dataset [18], which consists of eight diverse scenes. We define the test set by uniformly sampling 200 views on both a close and a far sphere around the scene center, totaling 400 images. This setup is the same as the camera space

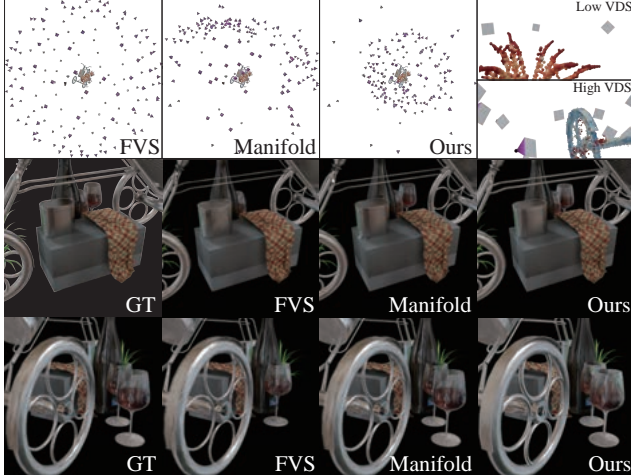


Figure 5. Qualitative comparison of optimized views. The fourth column in the first row visualizes the View-Dependency Scores (VDS) from two different point cameras, with blue indicating high VDS (high view dependency) and red indicating low VDS. The first three columns in the first row illustrate the final optimized views. The second and third rows present rendered images obtained from radiance fields reconstructed using these optimized views.

used in FVS and the initial views of Manifold Sampling. For each scene, our method begins with 20 initial views and optimizes additional 50 and 150 views. To ensure fair evaluation, we provide the same 20 initial views as additional views for FVS and Manifold Sampling.

Furthermore, we evaluate our method on large scale indoor scenes, *minimal room* and *indoor Christmas*, high-quality environments featuring distinct scene properties from BlenderKit [3]. The test set is constructed by randomly sampling 200 points on the surface of an ellipsoid that fits within the empty space of each indoor scene, with viewing directions aligned to the surface normals. For this BlenderKit dataset, we use 100 initial views and optimize 300 additional views. The results are compared with a baseline of randomly sampling 300 views from the volume.

7.2. Evaluation on View Optimization

We first compare our view optimization results with FVS and Manifold Sampling on NSVF dataset. The quantitative and qualitative comparisons are shown in Tables 1 and 2, and Figs. 5 and 8. Our method demonstrates superior performance in close-view reconstruction, as shown in Table 1. Remarkably, our method with 50 additional cameras outperforms both FVS and Manifold Sampling with both 50 and 150 additional views. Fig. 8 illustrates that our method captures intricate view-dependent appearances, such as metallic reflections in *Wine Holder* and detailed textures in *Still Life*. These results describe the advantage of continuous and unconstrained view optimization, especially under limited camera budgets. The slightly lower PSNR compared to the

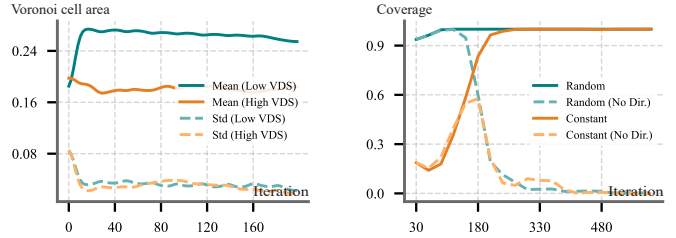


Figure 6. The left graph illustrates the Voronoi cell areas defined by optimized camera splats over training iterations, reflecting their directional sampling distribution. The right graph evaluates overall scene coverage across training iterations, comparing the results obtained with and without the directional regularizer.

baselines in far-view evaluations (Table 2) is attributed to pixel-level artifacts such as aliasing, whereas our method remains competitive in structural similarity metrics like SSIM and LPIPS.

As shown in Fig. 8, the optimized views from our framework are positioned closer to the scene compared to other methods. When 3DGS is trained using these close-up views, it may produce pixel-level artifacts, such as aliasing, when rendered from far-views. This results in slightly lower PSNR, a pixelwise metric, in far-view evaluations (Table 2). However, our method remains competitive in structural similarity metrics such as SSIM and LPIPS, indicating that the overall scene structure and appearance are well preserved.

The experiments on BlenderKit, the large indoor scenes, are shown in Table 3 and Fig. 9. Our method achieves higher reconstruction quality on the *Indoor Christmas* scene, which includes complex lighting and view-dependent materials, such as semi-transparent curtains. In *Minimal Room* scene, VDS makes minimal difference as the scene consists of low view-dependency regions, reducing the impact of view-dependent sampling.

Regarding optimization latency, FVS completes view selection in about 1 second, while Manifold Sampling takes approximately 1 hour on the NSVF dataset. Our method completes optimization in approximately 1 minute across all datasets, including the BlenderKit dataset with 300 optimized views. This demonstrates that our method is both scalable and efficient, making it suitable for a wide range of scene types and sizes.

7.3. Analysis of Camera Splatting

We validate our core rationale of directional adjustment guided by the View Dependency Score (VDS). We set up a proxy geometry of a sphere divided into two hemispheres, each assigned high and low VDS values, respectively. We measure the density and directional uniformity for each point camera with spherical Voronoi diagrams [4] of camera splats as shown in the left graph of Fig. 6. The results show higher density (smaller Voronoi cells) in the high-VDS region and lower density (larger Voronoi cells) in the low-

VDS region. The reduced standard deviation of cell areas confirms improved directional uniformity.

We evaluate the effectiveness of our directional regularizer in achieving global scene coverage. In this experiment, the camera splats are initialized in two ways, random positions oriented toward the scene center and identical positions and orientations. We measure the coverage ratio of point cameras for both initialization schemes, as shown in the right graph of Fig. 6. Our regularizer encourages camera splats to orient toward undersampled point camera, effectively maximizing coverage across the entire set while the optimization without directional regularizer fails to cover the scene.

We also provide a detailed qualitative analysis of optimized view placements and reconstruction results on the *wine holder* scene from the NSVF dataset (Fig. 5). Our method adaptively distributes camera views according to the local View Dependency Score (VDS). Views are densely placed around regions with high VDS, such as the metallic wheel, while fewer views are positioned around regions with low VDS, such as the diffuse box. This strategic allocation effectively enhances the quality of view-dependent appearance without compromising overall reconstruction accuracy.

7.4. Discussions

Robustness to the proxy geometry We evaluate the robustness of our method with respect to the quality of the proxy geometry. We optimize 3DGS scenes using varying numbers of initial input views, resulting in proxy geometries of different quality levels.

As shown in Table 4, view optimization fails when the proxy geometry is reconstructed with only 10 input views, as the the 3DGS contains severe artifacts such as floating blobs. These artifacts lead to poor *point camera* placement, degrading the view optimization process. In contrast, when using 20 or more input views, the proxy geometry contains far fewer artifacts, enabling successful view optimization. This experiment shows that our method consistently maintains high performance as long as the proxy geometry is not severely degraded.

Densification for camera splats While the 3DGS framework employs densification to progressively increase the number of Gaussians, our framework does not adopt densification for camera splats. This is because our target camera budget is predefined, and the coarse region of interest is already known from the proxy geometry. This allows us to initialize the camera splats in reasonable positions from the beginning. We then jointly optimize all camera splats simultaneously, eliminating the need for a separate densification step.

	10	20	50	100
PSNR \uparrow	25.55	29.63	29.21	28.95
SSIM \uparrow	0.863	0.929	0.929	0.925
LPIPS \downarrow	0.123	0.058	0.061	0.063

Table 4. Evaluation of the robustness of our method against the quality of proxy geometry, which is reconstructed using varying numbers of initial input views.

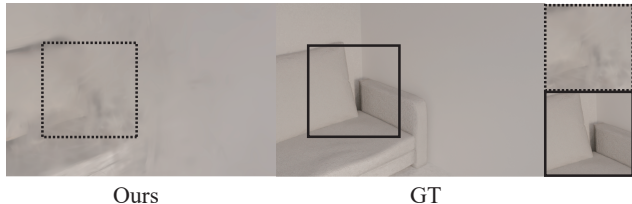


Figure 7. Illustration of a failure case caused by sparse initial geometry in a scene dominated by textureless regions.

Failure cases and future directions As we discussed earlier, significantly flawed proxy geometries can degrade optimization results. In some indoor scenes dominated by textureless regions such as uniformly colored walls, 3DGS tends to produce imbalanced distributions of Gaussian primitives, as illustrated in Fig. 7. Such failures lead to sparse 3D Gaussian distributions and imbalanced point camera placements, resulting in suboptimal view optimization quality. Future work could explore more robust proxy geometries, such as coarse geometric primitives, to mitigate these issues.

8. Conclusion

We introduce Camera Splatting, a novel gradient-based view optimization framework designed for radiance field reconstruction. Departing from discrete view sampling methods, Camera Splatting leverages continuous exploration of the joint view parameter space, effectively capturing complex view-dependent effects and covering entire scene geometry. Thanks to the computational efficiency of the Gaussian Splat rendering technique, our method achieves rapid evaluation of viewpoint quality, resulting in convergence within one minute, even during simultaneous batch optimization of a large number of views. Our framework provides highly informative views, facilitating more efficient and accurate radiance field reconstructions, beneficial across diverse scenarios and scene scales.

References

- [1] Jonathan T. Barron, Ben Mildenhall, Dor Verbin, Pratul P. Srinivasan, and Peter Hedman. Mip-nerf 360: Unbounded anti-aliased neural radiance fields. *CVPR*, 2022. 2
- [2] Christian Beder and Richard Steffen. Determining an initial image pair for fixing the scale of a 3d reconstruction from an

- image sequence. In *Joint Pattern Recognition Symposium*, pages 657–666. Springer, 2006. 3
- [3] BlenderKit, 2021. 7
- [4] Manuel Caroli, Pedro MM de Castro, Sébastien Lorient, Olivier Rouiller, Monique Teillaud, and Camille Wormser. Robust and efficient delaunay triangulations of points on or close to a sphere. In *Experimental Algorithms: 9th International Symposium, SEA 2010, Ischia Island, Naples, Italy, May 20–22, 2010. Proceedings 9*, pages 462–473. Springer, 2010. 7
- [5] Xiao Chen, Quanyi Li, Tai Wang, Tianfan Xue, and Jiangmiao Pang. Gennbv: Generalizable next-best-view policy for active 3d reconstruction. In *Proceedings of the IEEE/CVF Conference on Computer Vision and Pattern Recognition*, pages 16436–16445, 2024. 2
- [6] Enrique Dunn and Jan-Michael Frahm. Next best view planning for active model improvement. In *BMVC*, pages 1–11, 2009. 3
- [7] Xinyi Fan, Linguang Zhang, Benedict Brown, and Szymon Rusinkiewicz. Automated view and path planning for scalable multi-object 3d scanning. *ACM Transactions on Graphics (TOG)*, 35(6):1–13, 2016. 2
- [8] Sara Fridovich-Keil, Alex Yu, Matthew Tancik, Qinhong Chen, Benjamin Recht, and Angjoo Kanazawa. Plenoxels: Radiance fields without neural networks. In *Proceedings of the IEEE/CVF conference on computer vision and pattern recognition*, pages 5501–5510, 2022. 2
- [9] Wen Jiang, Boshu Lei, and Kostas Daniilidis. Fisherrf: Active view selection and uncertainty quantification for radiance fields using fisher information. *arXiv preprint arXiv:2311.17874*, 2023. 2, 3
- [10] Liren Jin, Xieyuanli Chen, Julius Rückin, and Marija Popović. Neu-nbv: Next best view planning using uncertainty estimation in image-based neural rendering. In *2023 IEEE/RSJ International Conference on Intelligent Robots and Systems (IROS)*, pages 11305–11312. IEEE, 2023. 3
- [11] James T Kajiya. The rendering equation. In *Proceedings of the 13th annual conference on Computer graphics and interactive techniques*, pages 143–150, 1986. 3
- [12] Alex Kendall and Yarin Gal. What uncertainties do we need in bayesian deep learning for computer vision? *Advances in neural information processing systems*, 30, 2017. 3
- [13] Bernhard Kerbl, Georgios Kopanas, Thomas Leimkühler, and George Drettakis. 3d gaussian splatting for real-time radiance field rendering. *ACM Trans. Graph.*, 42(4):139–1, 2023. 2, 3, 6
- [14] Georgios Kopanas and George Drettakis. Improving nerf quality by progressive camera placement for free-viewpoint navigation. 2023. 2, 3
- [15] Michael Krainin, Brian Curless, and Dieter Fox. Autonomous generation of complete 3d object models using next best view manipulation planning. In *2011 IEEE international conference on robotics and automation*, pages 5031–5037. IEEE, 2011. 2
- [16] Soomin Lee, Le Chen, Jiahao Wang, Alexander Liniger, Suryansh Kumar, and Fisher Yu. Uncertainty guided policy for active robotic 3d reconstruction using neural radiance fields. *IEEE Robotics and Automation Letters*, 7(4):12070–12077, 2022. 2, 3
- [17] Monica MQ Li, Pierre-Yves Lajoie, and Giovanni Beltrame. Frequency-based view selection in gaussian splatting reconstruction. *arXiv preprint arXiv:2409.16470*, 2024. 2
- [18] Lingjie Liu, Jiatao Gu, Kyaw Zaw Lin, Tat-Seng Chua, and Christian Theobalt. Neural sparse voxel fields. *Advances in Neural Information Processing Systems*, 33:15651–15663, 2020. 6, 11
- [19] Linjie Lyu, Ayush Tewari, Marc Habermann, Shunsuke Saito, Michael Zollhöfer, Thomas Leimkühler, and Christian Theobalt. Manifold sampling for differentiable uncertainty in radiance fields. In *SIGGRAPH Asia 2024 Conference Papers*, pages 1–11, 2024. 2, 3, 6
- [20] Miguel Mendoza, J Irving Vasquez-Gomez, Hind Taud, L Enrique Sucar, and Carolina Reta. Supervised learning of the next-best-view for 3d object reconstruction. *Pattern Recognition Letters*, 133:224–231, 2020. 2
- [21] Ben Mildenhall, Pratul P. Srinivasan, Matthew Tancik, Jonathan T. Barron, Ravi Ramamoorthi, and Ren Ng. Nerf: Representing scenes as neural radiance fields for view synthesis. In *ECCV*, 2020. 2, 3, 6
- [22] Richard A. Newcombe, Shahram Izadi, Otmar Hilliges, David Molyneaux, David Kim, Andrew J. Davison, Pushmeet Kohi, Jamie Shotton, Steve Hodges, and Andrew Fitzgibbon. Kinectfusion: Real-time dense surface mapping and tracking. In *2011 10th IEEE International Symposium on Mixed and Augmented Reality*, pages 127–136, 2011. 6
- [23] Xuran Pan, Zihang Lai, Shiji Song, and Gao Huang. Activenerf: Learning where to see with uncertainty estimation. In *European Conference on Computer Vision*, pages 230–246. Springer, 2022. 2, 3
- [24] Yunlong Ran, Jing Zeng, Shibo He, Jiming Chen, Lincheng Li, Yingfeng Chen, Gimhee Lee, and Qi Ye. Neurar: Neural uncertainty for autonomous 3d reconstruction with implicit neural representations. *IEEE Robotics and Automation Letters*, 8(2):1125–1132, 2023. 3
- [25] Mike Roberts, Debadeepta Dey, Anh Truong, Sudipta Sinha, Shital Shah, Ashish Kapoor, Pat Hanrahan, and Neel Joshi. Submodular trajectory optimization for aerial 3d scanning. In *International Conference on Computer Vision (ICCV) 2017*, 2017. 2, 3
- [26] Luca Savant, Diego Valsesia, and Enrico Magli. Modeling uncertainty for gaussian splatting. *arXiv preprint arXiv:2403.18476*, 2024. 3
- [27] William R Scott, Gerhard Roth, and Jean-François Rivest. View planning for automated three-dimensional object reconstruction and inspection. *ACM Computing Surveys (CSUR)*, 35(1):64–96, 2003. 2
- [28] Neil Smith, Nils Moehle, Michael Goesele, and Wolfgang Heidrich. Aerial path planning for urban scene reconstruction: A continuous optimization method and benchmark. 2018. 2, 3
- [29] Niko Sünderhauf, Jad Abou-Chakra, and Dimity Miller. Density-aware nerf ensembles: Quantifying predictive uncertainty in neural radiance fields. In *2023 IEEE International Conference on Robotics and Automation (ICRA)*, pages 9370–9376. IEEE, 2023. 3

- [30] Wenhui Xiao, Rodrigo Santa Cruz, David Ahmedt-Aristizabal, Olivier Salvado, Clinton Fookes, and Leo Lebrat. Nerf director: Revisiting view selection in neural volume rendering. In *Proceedings of the IEEE/CVF Conference on Computer Vision and Pattern Recognition*, pages 20742–20751, 2024. [2](#), [6](#)
- [31] Zimu Yi, Ke Xie, Jiahui Lyu, Minglun Gong, and Hui Huang. Where to render: Studying renderability for ibr of large-scale scenes. In *2023 IEEE Conference Virtual Reality and 3D User Interfaces (VR)*, pages 356–366. IEEE, 2023. [3](#)
- [32] Huangying Zhan, Jiyang Zheng, Yi Xu, Ian Reid, and Hamid RezaTofighi. Activermap: Radiance field for active mapping and planning. *arXiv preprint arXiv:2211.12656*, 2022. [2](#)
- [33] Xiaohui Zhou, Ke Xie, Kai Huang, Yilin Liu, Yang Zhou, Minglun Gong, and Hui Huang. Offsite aerial path planning for efficient urban scene reconstruction. *ACM Transactions on Graphics (TOG)*, 39(6):1–16, 2020. [2](#), [3](#)

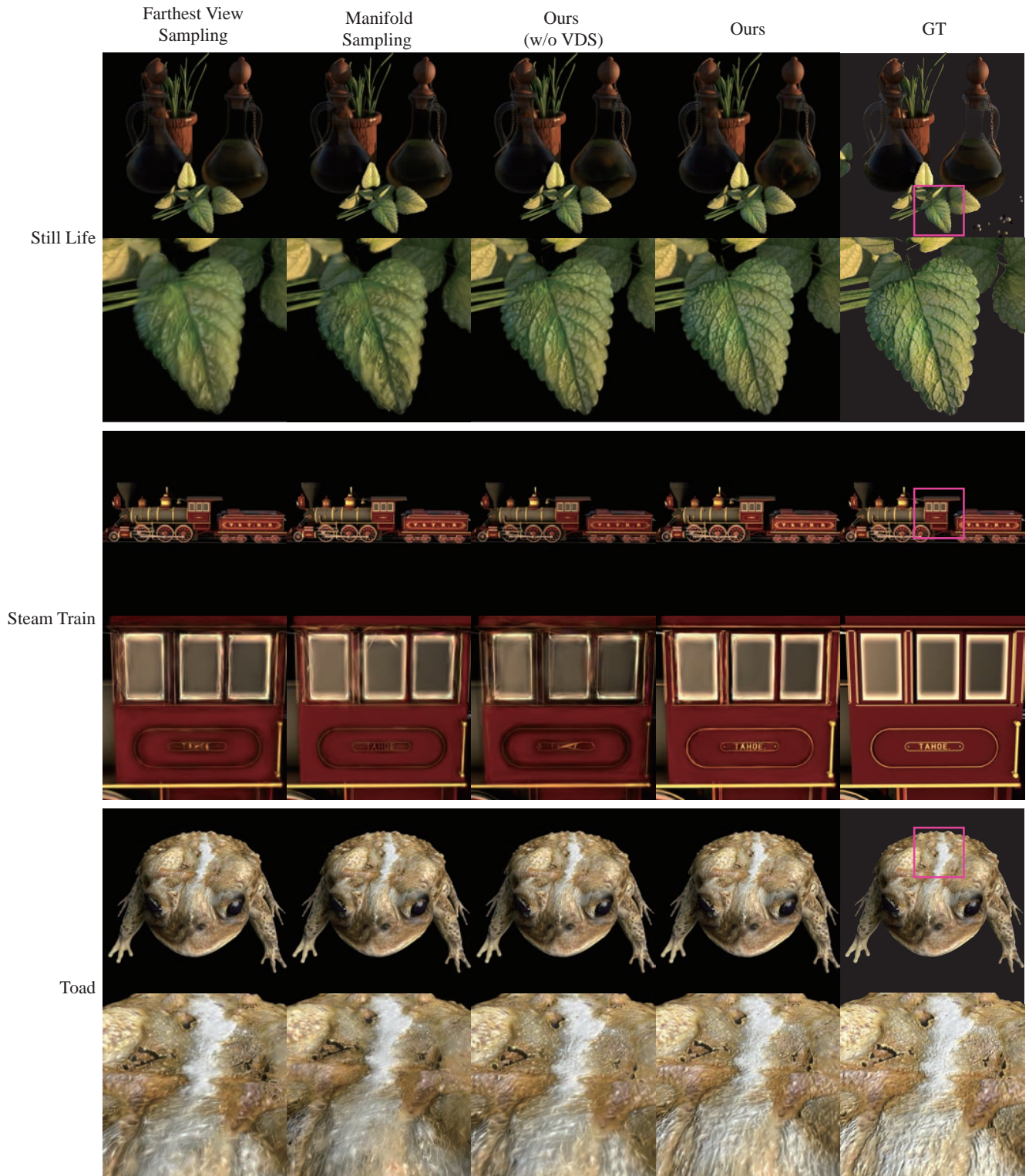


Figure 8. Qualitative evaluation on the Synthetic-NSVF dataset [18]. The first row shows renderings from optimized views that show the overall scenes from a distant perspective. The second row provides close-up renderings of the regions highlighted by pink squares, our view optimization successfully captures detailed radiance fields and intricate view-dependent appearances.

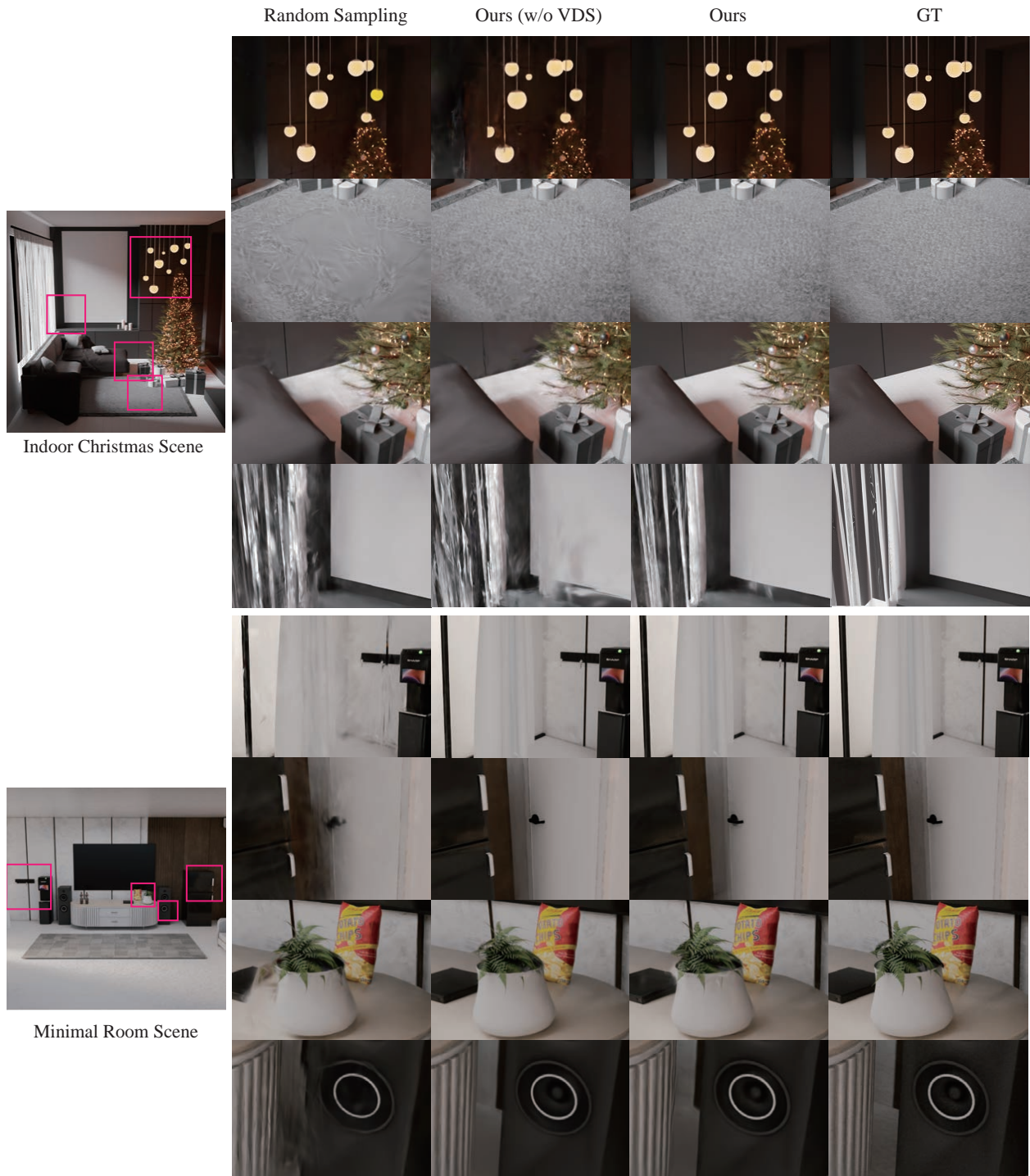


Figure 9. Qualitative evaluation on the BlenderKit dataset. Each row shows close-up renderings corresponding to regions highlighted by pink squares in the first column images. Radiance fields reconstructed using our optimized viewpoints effectively capture detailed geometry and complex view-dependent appearances.